PROCEEDINGS OF SPIE

SPIEDigitalLibrary.org/conference-proceedings-of-spie

Curved primary aperture segmentation enabling a robust quasi-Airy pattern point spread function

Kevin Z. Derby, James B. Breckinridge, James E. Harvey, Tony Hull, Charles F. Lillie, et al.

Kevin Z. Derby, James B. Breckinridge, James E. Harvey, Tony Hull, Charles F. Lillie, Jaren N. Ashcraft, Heejoo Choi, Ewan S. Douglas, Daewook Kim, "Curved primary aperture segmentation enabling a robust quasi-Airy pattern point spread function," Proc. SPIE 12188, Advances in Optical and Mechanical Technologies for Telescopes and Instrumentation V, 121880N (29 August 2022); doi: 10.1117/12.2628819

SPIE.

Event: SPIE Astronomical Telescopes + Instrumentation, 2022, Montréal, Québec, Canada

Curved primary aperture segmentation enabling a robust quasi-Airy pattern point spread function

Kevin Z. Derby[a], James B. Breckinridge[a], James E. Harvey[b], Tony Hull[c], Charles F. Lillie[d], Jaren N. Ashcraft[a], Heejoo Choi[a,e], Ewan S. Douglas[f], and Daewook Kim[a,e,f]

[a]Wyant College of Optical Sciences, University of Arizona, Tucson, AZ, USA
[b]Photon Engineering LLC, 310 S Williams Blvd, Tucson, AZ, USA
[c]Department of Physics and Astronomy, University of New Mexico, Albuquerque, NM, USA
[d]Lillie Consulting LLC, 6202 Vista Del Mar, Playa Del Rey, CA, USA
[e]Large Binocular Telescope Observatory, University of Arizona, Tucson, AZ, USA
[f]Department of Astronomy and Steward Observatory, University of Arizona, Tucson, AZ, USA

ABSTRACT

Future NASA flagship missions will require the collecting area and resolving power of 6 meter or larger aperture telescopes. Due to limits in fairing size, highly accurate and stable segmented primary mirrors are desirable for achieving these apertures. Due to periodic discontinuities, hexagonally segmented mirrors have intrinsic diffraction grating-like structures, causing pronounced starburst point spread functions (PSFs). To mitigate unwanted image plane diffraction, we have designed and simulated a novel curved-edge segmentation method, called pinwheel segmentation, which more closely emulates a filled circular primary aperture.

A parametric solution space for pinwheel segmentation has been developed and used to create in-house Python code which can be integrated with two optical propagation software: Physical Optics Propagation in Python (POPPY) and High Contrast Imaging in Python (HCIPy). Using HCIPy, we demonstrate optimized pinwheel design solutions which are less sensitive to realistic degradation scenarios on-orbit such as optical surface errors and beamwalk due to observatory pointing errors. Additionally, to demonstrate its potential benefits for high-contrast astrophysics, coronagraphy was compared using 6-meter class hexagonal and pinwheel segmented primary mirrors. Preliminary results demonstrate the advantages of alternative segmentation geometries when degraded PSFs are considered. The increased performance and robustness of pinwheel segmentation have the potential of significantly increasing science returns for future missions while reducing spacecraft operational constraints and cost.

Keywords: Mirror segmentation, pinwheel, physical optics modeling, coronagraphy, high contrast imaging

1. INTRODUCTION

Future space telescope missions will require the collecting area and resolving power of 6 meter or larger primary mirrors. However, due to limits in manufacturing and rocket fairing size, monolithic primary mirrors are not feasible. Thus, highly accurate and stable segmented primary mirrors desirable for achieving large apertures.[1] Future NASA flagships such as the ultraviolet optical infrared (UVOIR) observatory baseline hexagonally segmented primary mirrors.[2] These hexagonal segmented apertures have three sets of straight segment edges which form diffraction grating-like structures which diffract the incoming wavefront along three respective axes in the corresponding Fourier space, leading to a six-pointed starburst point spread function (PSF) shown in Figure 1. These diffraction spikes can mask faint astrophysical objects, crowded targets, or high-contrast objects of interest. Additionally, they can contaminate stellar or exoplanet spectra, requiring complex data processing algorithms[3,4] or exotic apodizing masks to achieve high performance.[5–7]

Further author information: (Send correspondence to D.K.)
D.K.: E-mail: dkim@optics.arizona.edu

Advances in Optical and Mechanical Technologies for Telescopes and Instrumentation V,
edited by Ramón Navarro, Roland Geyl, Proc. of SPIE Vol. 12188, 121880N
 · 0277-786X · doi: 10.1117/12.2628819

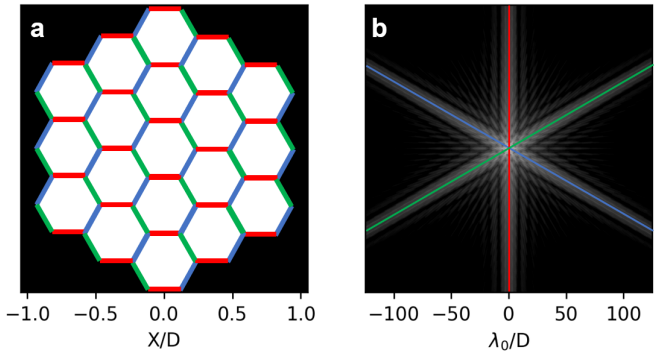

Figure 1. (a) A 6.5 meter diameter hexagonal segmented aperture. Segment edges are highlighted to show the three sets of diffraction grating-like structures formed. (b) These diffract the incident wavefront (λ_0 = 550 nm, 20% bandwidth) along three respective axes in the corresponding image plane. The image shown is normalized and logarithmically scaled.

For future large field of view space telescopes especially, intrinsic field-dependent aberrations will create non-linear shift invariant (non-LSI) PSFs across the image plane. These non-LSI PSFs, in addition to signal-dependent shot noise, make image processing challenging and fundamentally uncertain. Another side effect of starburst PSFs is their high slope in both amplitude and phase when considering the electric field at the focal plane, as small perturbations will lead to large changes in the PSF, which is the modulus squared of the electric field. This leaves the system vulnerable to degradations caused by fluctuating thermal gradients,[8] beamwalk on intermediate optics due to pointing errors,[9] or optical surface errors.[10]

A chief goal for future NASA missions is to directly image and characterize Earth-like exoplanets to search for signatures of life. However, these planets are typically 10^{10} times fainter than, and separated by fractions of an arcsecond from their host star.[11,12] To achieve these extreme contrasts, coronagraphs are used to attenuate starlight and allow for exoplanet detection at small separations.[13,14] For hexagonally segmented telescopes a combination of active deformable mirror (DM) control, complex apodizers, and focal plane masks are required to suppress diffraction flares caused by the gaps between mirror segments.[15]

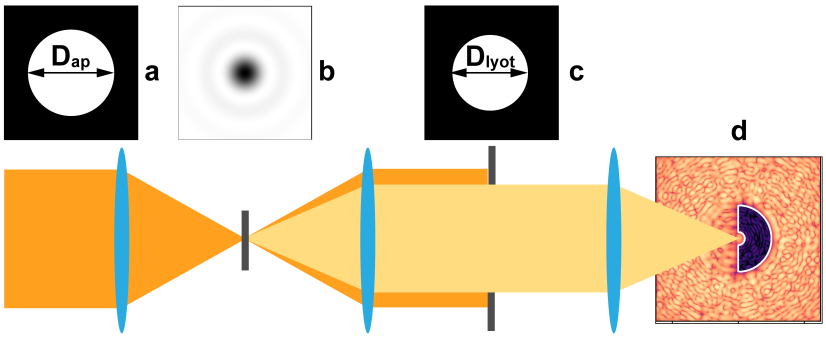

Figure 2. Basic coronagraph instrument layout. (a) The input wavefront with diameter D_{ap} is corrected by a DM and sent to a (b) focal plane mask. A sinc-squared band-limited occulter is used in this example. This diffracts on-axis starlight to the outer edge of the pupil, which is blocked by an undersized (c) Lyot stop with diameter D_{lyot}. Residual starlight and off-axis light from exoplanets or debris disks makes it through the Lyot stop to the (d) final science image. The science image has a representative dark hole dug from 2 to 10 λ/D.

Several methods of compensation for these errors using closed-loop wavefront control have been introduced, including stroke minimization and electric field conjugation algorithms.[16–18] These calculate the DM shape required to minimize the amount of residual starlight within a specified region of the image known as the "dark hole".

Physical Optics Propagation in Python (POPPY)[19] and High Contrast Imaging in Python (HCIPy)[20] are

open-source Python libraries primarily developed by teams of astronomers at the Space Telescope Science Institute and Leiden University respectively. They are open to contributions from scientists and software developers around the world, and are used to simulate physical optics propagation. They propagate the complex electromagnetic wavefront through the optical system using either the Fraunhofer or Fresnel approximations of scalar electromagnetic theory. In-house Python code compatible with both POPPY and HCIPy has been developed to create pinwheel apertures and model its diffraction effects in the context of astronomical telescopes and coronagraphs.

In the following sections, we present an overview of pinwheel segmentation, and for the first time define a parameterized solution space for constructing pinwheel apertures. We analyze these parameters and their impact on the PSF. Additionally, we model two UVOIR-like telescopes as suggested in the 2021 Decadal Survey.[1] Using these models, we demonstrate a dark hole dug using a pinwheel aperture, and compare its performance to a hexagonally segmented aperture in the presence of on-orbit degredations.

2. PINWHEEL SEGMENTATION

In this section, we give a overview of the theory behind and define a parameterized solution space for pinwheel segmented apertures.

2.1 Theory and Construction

Astronomers have demonstrated the use of curved secondary mirror spiders to minimize diffraction effects since the mid twentieth century.[21] Fraunhofer diffraction theory has since been applied to show that pupil obscurations in the form of circular arcs result in fanned out "searchlight" or "bow-tie" diffraction flares.[22] These diffraction flares subtend the same angle as the circular arc used to create them, but in two directions. This can be intuitively understood using Fourier theory by dividing the arc into many smaller straight-line segments.[23] Thus, if the arc is a semicircle (or an integer multiple thereof) the resulting diffraction pattern would simply be a complete circle, resulting in the suppression of unwanted image plane diffraction spikes. Pinwheel segmentation builds upon this by using inscribed circular arcs as spokes to slice an aperture into azimuthal segments.[24–28] As long as the combination of these spokes constitutes an integer multiple of a semicircle, the result will be an azimuthally symmetric, quasi-airy PSF (Figure 3).

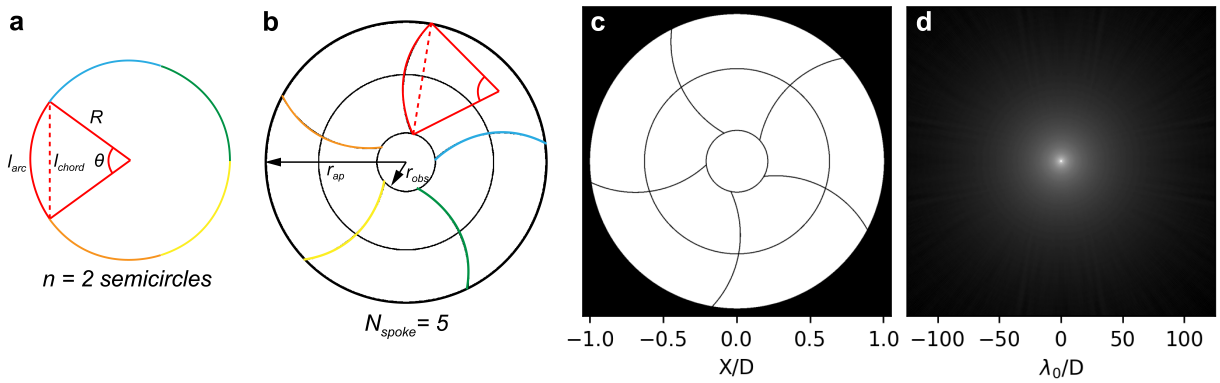

Figure 3. (a) A complete circle (2 semicircles) is broken into 5 arcs which are used to inscribe (b) a 5-spoke pinwheel segmented aperture with radius r_{ap} and a central segment with radius r_c. (c) The same 5-spoke pinwheel modeled as a 6.5 meter diameter unobscured aperture. (d) An incident wavefront ($\lambda_0 = 550$ nm, 20% bandwidth) is propagated through the pinwheel aperture and creates an azimuthally-symmetric, quasi-Airy PSF.

This boundary condition imposes a discrete solution space for pinwheel segmented apertures based on aperture geometry and the desired number of segments. To construct a pinwheel aperture, we begin by definining the number of spokes (N_{spoke}) or inscribed arcs with length (l_{arc}). This slices the aperture into a set number of azimuthal segments which can be scaled up through the introduction of annular rings. We know that these inscribed arcs when translated and set end-to-end, must constitute an integer multiple (n) of a semicircle with radius R:

$$l_{arc} N_{spoke} = n\pi R\,, \tag{1}$$

l_{arc} is also defined by the central angle inscribed by a spoke (θ) and R:

$$l_{arc} = \theta R\,, \tag{2}$$

By combining Eqs. (1) and (2), we can solve for θ:

$$\theta = \frac{\pi n}{N_{spoke}}\,, \tag{3}$$

However, what we need is R. To find this, we first assume the chord (l_{chord}) spanned by each spoke is equal to the difference between the aperture radius (r_{ap}) and central segment radius (r_c):

$$l_{chord} = r_{ap} - r_c\,, \tag{4}$$

l_{chord} is also defined by the R and θ:

$$l_{chord} = 2R \sin\frac{\theta}{2}\,, \tag{5}$$

By combining Eqs. (4) and (5), then solving for the R, we get:

$$R = \frac{r_{ap} - r_c}{2\sin\left(\theta/2\right)}\,, \tag{6}$$

Finally, combining Eqs. (3) and (6) gives:

$$R = \frac{r_{ap} - r_c}{2\sin\left(\pi n/2N_{spoke}\right)}\,, \tag{7}$$

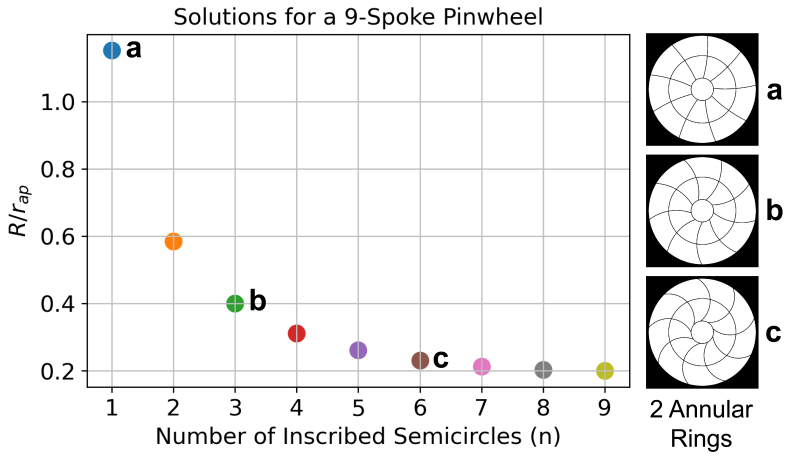

Figure 4. Solution space for a 9-spoke pinwheel aperture with aperture radius r_{ap} and a segment with radius $r_c = 0.2r_{ap}$. Example pinwheel segmented apertures that use (a) 1, (b) 3, and (c) 6 inscribed semicircles to create spokes are shown as well.

With r_{ap} and r_c set by aperture geometry, this leaves n and N_{spoke} as free parameters when segmenting a pinwheel aperture. N_{spoke} defines the number of segments, and as stated previously can be scaled up through the introduction of annular rings. n controls spoke curvature, as a smaller value corresponds to fewer semicircles the

spokes combine into, which leads to each arc constituting a smaller portion of a semicircle. Note that the values n can take range from 1 to N_{spoke}, which corresponds to each spoke being a complete semicircle. An example solution space for a 9-spoke pinwheel aperture with aperture radius r_{ap} and a segment with radius $r_c = 0.2r_{ap}$ is shown in Figure 4.

2.2 Point Spread Function Analysis

We demonstrate the effects of changing n, N_{spoke}, and gap width on a pinwheel PSF. Unobscured pinwheel apertures measuring 6 meters in diameter (D) were modeled as binary apodizing masks using in-house Python code compatible with HCIPy and POPPY. Each aperture contained two annular rings and had a central segment with diameter $D/5$. Unaberrated, monochromatic PSFs ($\lambda_0 = 550$ nm) were modeled for each aperture using Fraunhofer diffraction in HCIPy. Normalized and logarithmically scaled images of PSF irradiance are presented for qualitative comparison of PSFs. Additionally, azimuthally averaged radial plots of PSF irradiance are presented. These plots show azimuthal variations by plotting colored regions corresponding to one standard deviation (σ) above and below the mean irradiance.

First, we show how changing N_{spoke} impacts the PSF. Pinwheel apertures with 5, 9, and 15 spokes were modeled. For these apertures, gap width was kept constant at $D/2000$. In addition, n was set to 1, corresponding to the least curved spoke solution for each aperture. Figure 5 shows each aperture along with a corresponding PSF images and radial plots.

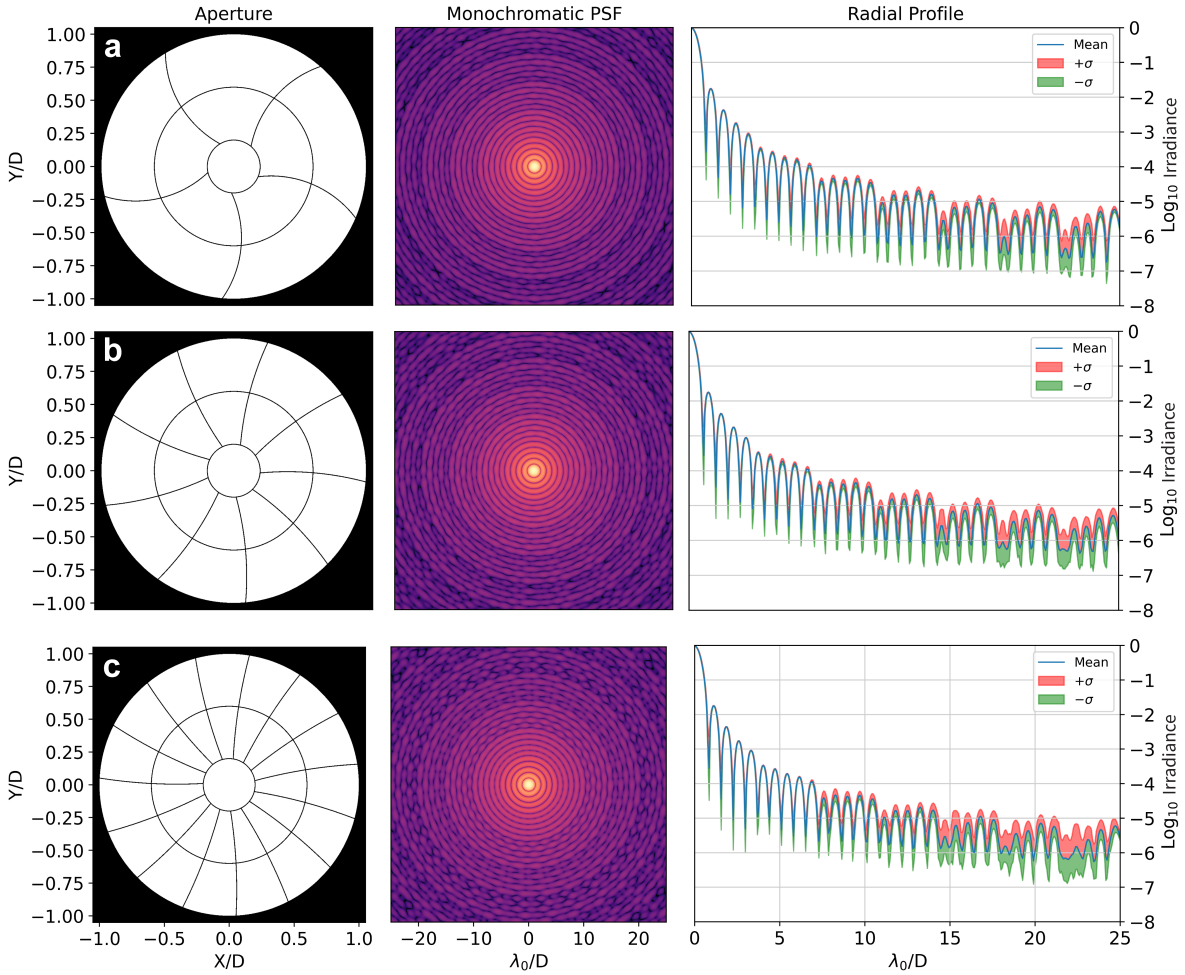

Figure 5. (a) 5-Spoke, (b) 9-spoke, and (c) 15-spoke pinwheel apertures.

We can see that as N_{spoke} increases, the PSF remains unchanged within the first 9 airy rings. However, past this point, we can see ovular lobes which become more distinct as N_{spoke} increases. This is reflected in the radial profiles which show the standard deviation increasing with N_{spoke} the further you are from the center of the PSF. This shows that N_{spoke}, or in general the total number of segments, should be kept to a minimum to limit these diffraction artifacts. This makes intuitive sense because fewer segments means fewer segment edges for the light to diffract off of, decreasing the amount of diffraction artifacts.

Next, we show how changing n, or spoke curvature, impacts the PSF. 9-spoke ($N_{spoke} = 9$) pinwheel apertures with n equal to 1, 3, and 5 were modeled. For these apertures, gap width was kept constant at $D/2000$. Figure 6 shows each aperture along with a corresponding PSF images and radial plots.

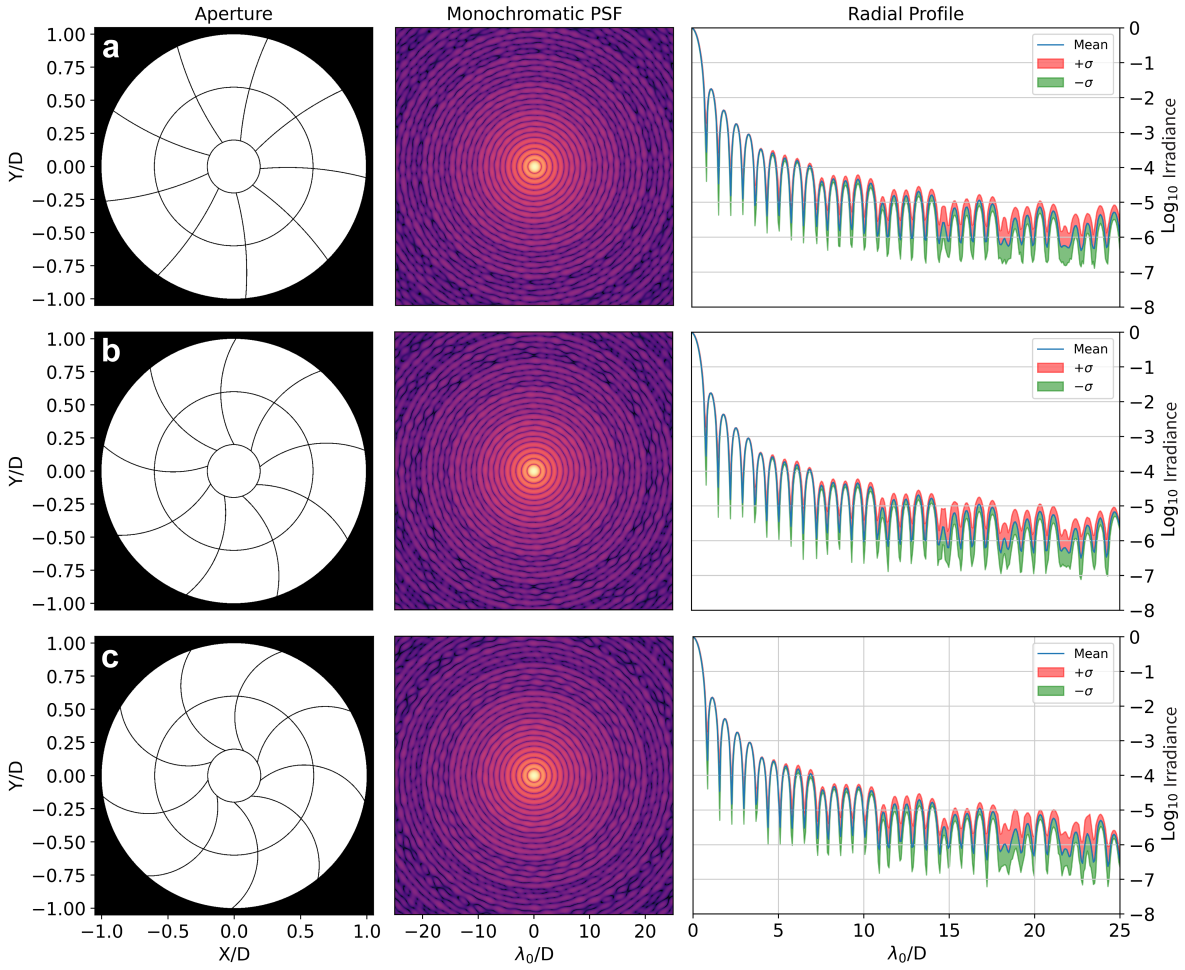

Figure 6. 9-Spoke pinwheel apertures that use (a) 1, (b) 3, and (c) 5 total semicircles to create spokes.

We can see that as n increases, the PSF remains relative unnaffected. This can also be seen in the radial profiles which not only have similar shapes, but similar deviations as well. Each of these apertures fulfills the primary boundary condition of having the spokes constitute an integer multiple of a semicircle. Thus, one might expect spoke curvature to not have a significant impact on the PSF. However, in the real-world, spoke curvature would likely be minimized for ease of manufacturability.

Lastly, we show how gap width between segments impacts the PSF. 9-spoke ($N_{spoke} = 9$) pinwheel apertures with $n = 1$ and gap widths corresponding to $D/2000$, $D/5000$, and $D/10000$ were modeled. Figure 7 shows each aperture along with a corresponding PSF images and radial plots.

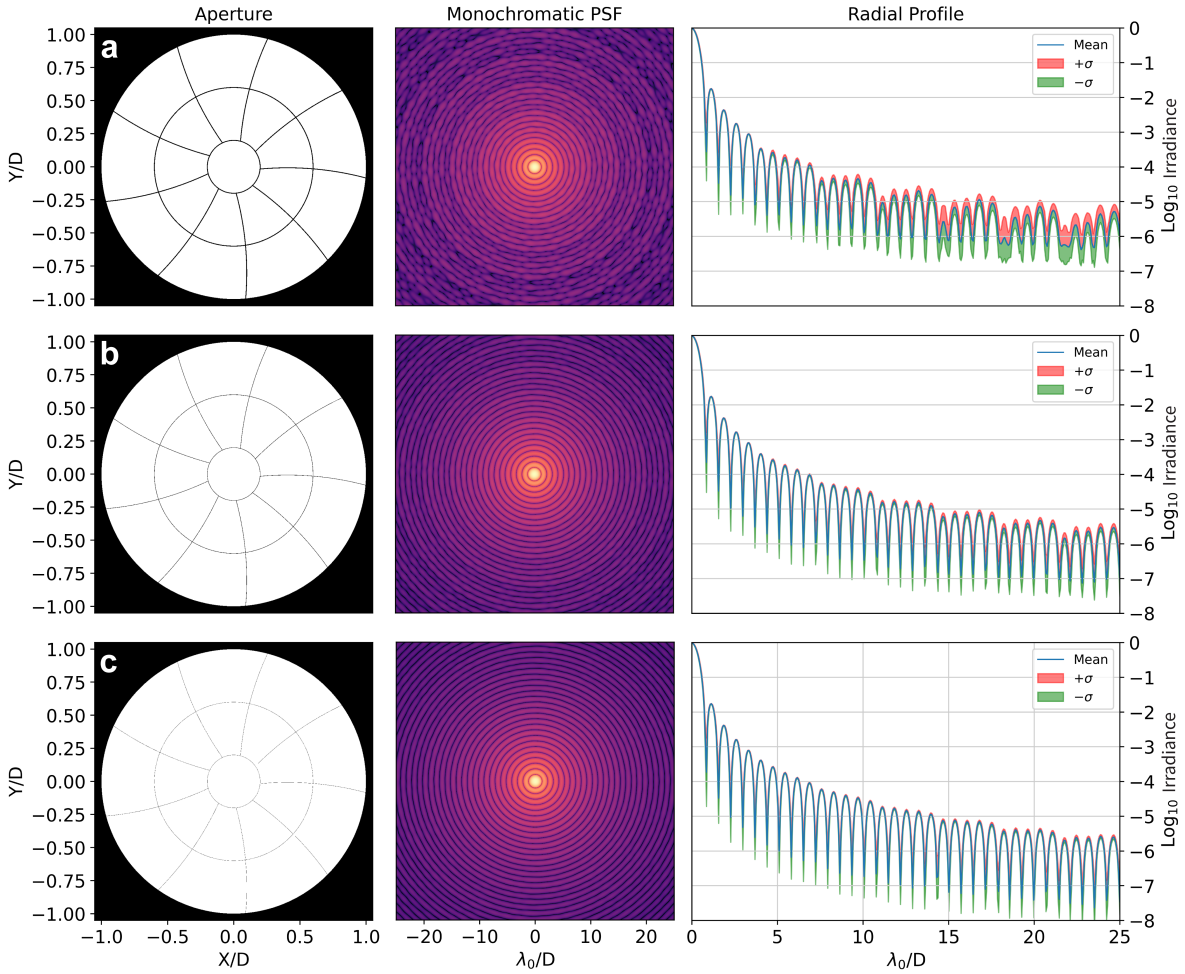

Figure 7. 9-Spoke pinwheel apertures with $n = 1$ and gap widths set at (a) $D/2000$, (b) $D/5000$, and (c) $D/10000$.

We can see that changing the gap width between segments has the most pronounced effect on the PSF. As the gap width decreases, the PSF becomes more azimuthally-symmetric. At a gap width of $D/10000$, which for $D = 6$ meters corresponds to 600 microns, the PSF is nearly indistinguishable from a standard Airy pattern. This is reflected in the radial profiles which show the standard deviation decreasing to near zero with a shape similar to an Airy pattern at smaller gap widths. As the reason for using a pinwheel aperture is to emulate an Airy pattern as close as possible, this shows that we want to keep gap width to a minimum.

3. CORONAGRAPHY SIMULATIONS AND ANALYSIS

Telescope and Lyot coronagraph models were created in Python using HCIPy. These were used to compare the performance between systems which use pinwheel and hexagonal segmentation in the presence of realistic on-orbit degredations.

3.1 Telescope and Instrument Model

Two unobscured, 6 meter diameter telescopes were modeled in Python using HCIPy. One used pinwheel segmentation to split the aperture into 19 segments using 9 spokes and 2 annular rings. The radius used to create spokes was set to 6.9 meters, corresponding to the least curved solution. The other model used hexagonal segmentation to split the aperture into 19 segments measuring 1.3 meters from flat-to-flat. The gap width between segments for both apertures was set to $D/2000$, corresponding to 1 millimeter.

In each model, a 550 nm wavefront was first sent a binary aperture mask. A phase screen was then used to inject 5 nanometers RMS of wavefront error. This aberrated telescope wavefront was then corrected by a 48 by 48 actuator DM. The corrected wavefront was then propagated to a focal plane mask and Lyot stop for starlight rejection. For the focal plane mask, a sinc-squared band-limited occulter with the first zero set at 6 first zero λ_0/D was used. The Lyot stop for each aperture measured $0.9D$ in diameter and had the gap width between segments scaled up by a factor of 20. The aperture, focal plane mask, and Lyot stop for each system is shown in Figure 8.

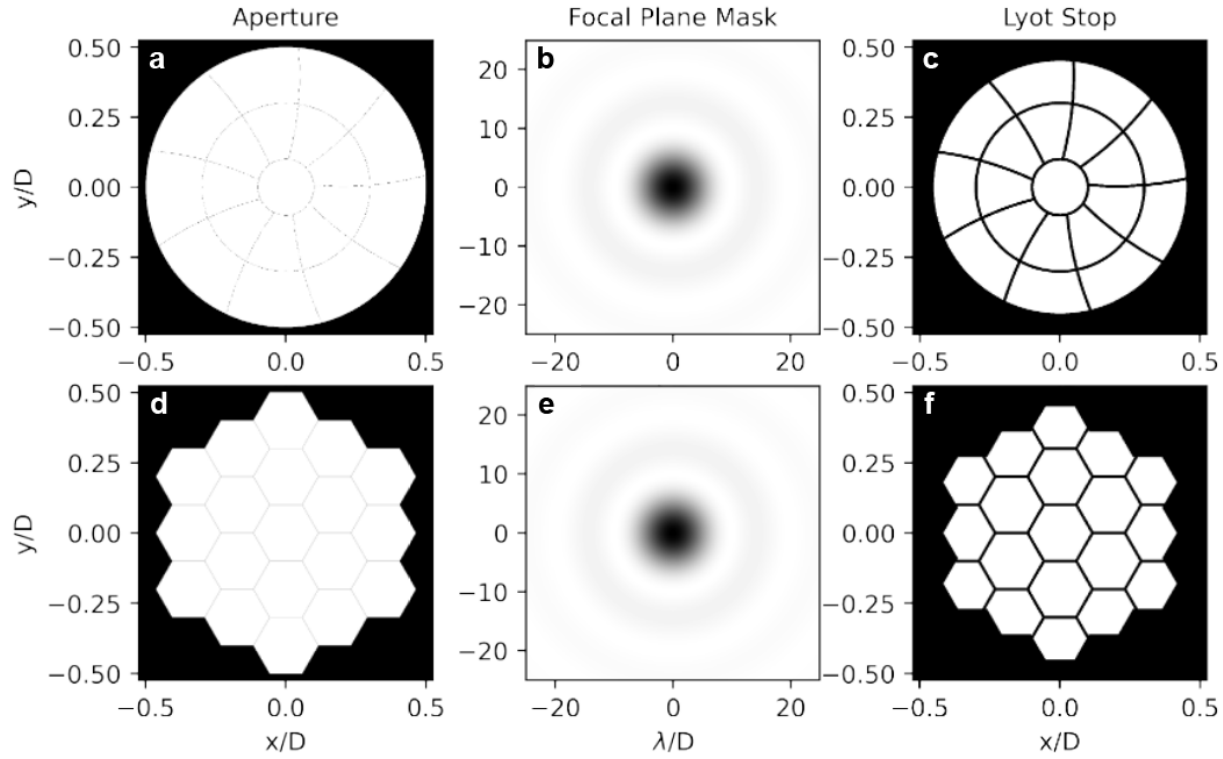

Figure 8. (a) A 6 meter pinwheel segmented aperture. Gap widths were set at 3 millimeters. (b) A sinc-squared band-limited occulter was used as a focal plane mask. (c) The pinwheel segmented Lyot stop measured $0.9D$ meters in diameter and had gap widths scaled up by a factor of 20. (d) A 6 meter hexagonal segmented aperture. Each segment measured 1.3 meters flat-to-flat and had gap widths set at 3 millimeters. (e) The same band-limited occulter was used as a focal plane mask. (f) The hexagonal segmented Lyot stop measured $0.9D$ meters in diameter and had gap widths scaled up by a factor of 20.

3.2 Coronagraphy Simulation Results

EFC using Tikhonov Regularization[18] was used to dig half of an annular dark hole between 2 and 10 λ/D for each aperture. A half dark hole was dug due to the use of only one DM, which only allows for correction of amplitude and phase errors in one half of the field. Other coronagraphs may use two DMs for correction of amplitude and phase errors across the whole field.[29] Future work may explore digging a full dark hole using two DMs. Once a dark hole was established, temporal degradation caused by beamwalk was then simulated. From the starting point, 100 random draws were taken from a Gaussian distribution with a standard deviation of 10 milli-arcseconds pointing error. These pointing errors were converted by assuming 1 millimeter of beamwalk per arcsecond. This was used to shift the phase screen before re-propagating the wavefront through the system. These 100 images were averaged together for a final dark hole which includes starlight leakage due to beamwalk.

In the presence of these degradations, the pinwheel aperture dark hole reached a lower average contrast of 3.9×10^{-10} contrast compared to the hexagonal aperture dark hole which reached an average contrast of

9.7×10^{-10}. Both apertures had similar standard deviations in dark hole contrast. Dark hole images and azimuthally averaged radial plots of dark hole contrast are presented in Figure 9. These plots show azimuthal variations by plotting colored regions corresponding to one standard deviation (σ) above and below the mean contrast.

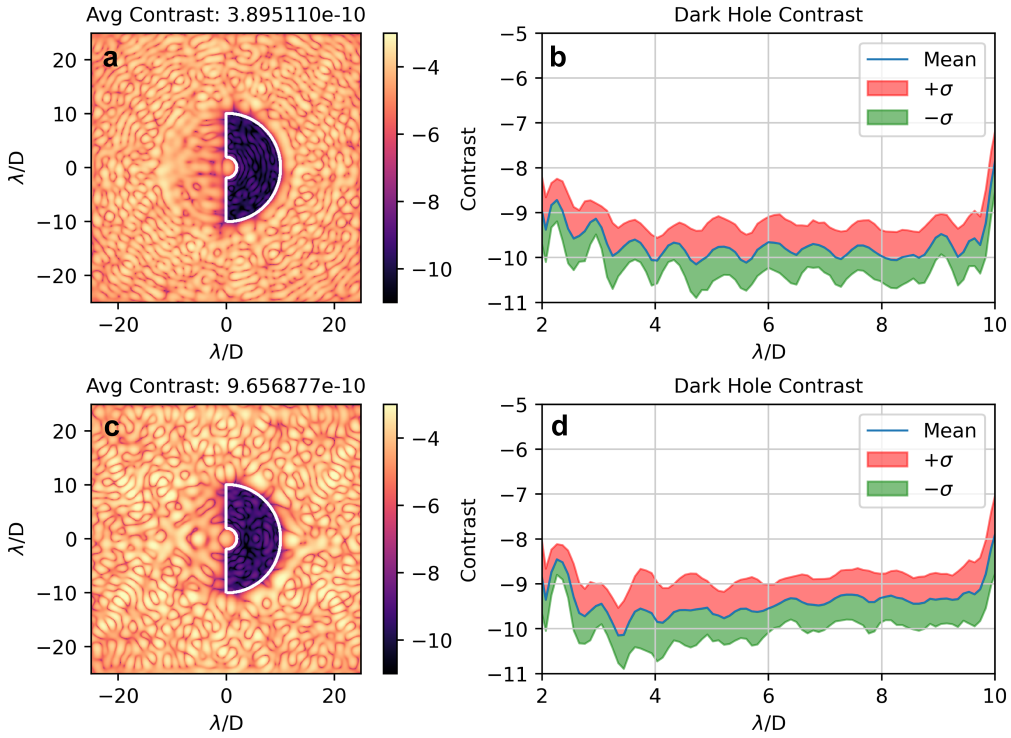

Figure 9. (a) A dark hole dug using EFC for a pinwheel segmented aperture. (b) A radial plot of contrast within the dark hole is also shown. (c) A dark hole dug using EFC for a hexagonally segmented aperture. (b) A radial plot of contrast within the dark hole is also shown.

While these preliminary results are promising, future work is needed to fully compare performance and robustness between pinwheel aperture coronagraphs and the more advanced coronagraphs being developed for future flagship missions. We expect a pinwheel aperture to be more robust to degradation thanks to its gentler slopes in amplitude and phase when considering the complex PSF.

3.3 Future Coronagraphy Analysis

Vector vortex phase plates present an attractive alternative to standard occulting focal plane masks due to their smaller inner working angles, higher throughput, and completely clear off-axis discovery space.[30] Additionally, advanced coronagraph designs such as the apodized pupil Lyot coronagraph[5,31] (APLC) or phase-induced ampliltude apodization complex mask coronagraph[32] (PIAACMC) require pupil shaping using complex apodizing masks to achieve high contrasts. We believe the use of a pinwheel aperture may bypass the need for pupil shaping thanks to its inherently quasi-Airy PSF.

As a preliminary demonstration, we show how a pinwheel aperture achieves a "circularized" intensity distribution in the Lyot plane when paired with a charge-6 vector vortex. This is in stark contrast to the hexagonal aperture case which would require pupil shaping due to diffraction caused by hexagonal segments. Future work will explore creating pinwheel segmented vector vortex coronagraphs without the need for apodizing masks. This would enable more robust and less complex coronagraph designs for increased throughput and science yield on future flagship missions.

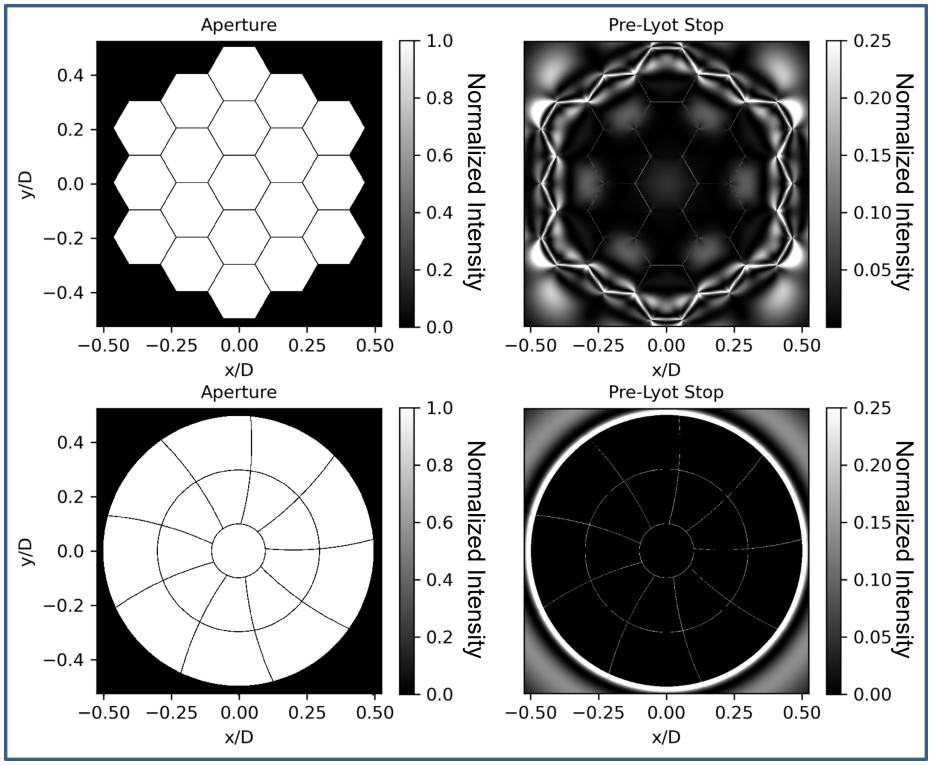

Figure 10. Pinwheel and hexagonally segmented apertures were paired with a charge-6 vector vortex phase plate to create vector vortex coronagraphs. Normalized intensity plots are shown to demonstrate how pinwheel segmentation achieves a "circularized" intensity distribution in the Lyot plane without the need for apodizers.

4. CONCLUSION

In this work, we present an overview of pinwheel segmentation, and for the first time define a parameterized solution space for constructing pinwheel apertures. We analyze the impact of N_{spoke}, n, and gap width between segments on the PSF. We show that minimizing gap width is the most important parameter in accurately emulating the Airy pattern given by a monolithic circular aperture.

In addition, we modeled two unobscured 6 meter telescope and Lyot coronagraph instruments. Using these models, we demonstrate dark holes dug using pinwheel and hexagonally segmented apertures. Our preliminary results demonstrate deeper dark hole contrast for a pinwheel aperture in the presence of 5 nanometer RMS surface error and beamwalk caused by 10 milli-arcseconds RMS pointing error. Future work will explore using pinwheel segmentation for more robust and less-complex coronagraphs designs, further advancing a key technology in the search for life beyond our solar system.

ACKNOWLEDGMENTS

The authors would like to acknowledge the help of other members within both the Large Optics Fabrication and Testing Group and University of Arizona Space and Astrophysics Lab. Special thanks to Maxim Duque for his assistance with simulations. We would also like to thank Kian Milani and Sebastiaan Haffert for their insight on setting up simulations using POPPY and HCIPy.

REFERENCES

[1] Decadal Survey on Astronomy and Astrophysics 2020 (Astro2020), Space Studies Board, Board on Physics and Astronomy, Division on Engineering and Physical Sciences, and National Academies of Sciences, En-

gineering, and Medicine, [*Pathways to Discovery in Astronomy and Astrophysics for the 2020s*], National Academies Press, Washington, D.C. (2021). Pages: 26141.

[2] Bolcar, M. R., Aloezos, S., Bly, V. T., Collins, C., Crooke, J., Dressing, D., Fantano, L., Feinberg, L. D., France, K., Gochar, G., Gong, Q., Jones, A., Linares, I., Postman, M., Pueyo, L., Roberge, A., Sacks, L., Tompkins, S., and West, G., "The Large UV/Optical/Infrared Surveyor (LUVOIR): Decadal Mission Concept Design Update," 24.

[3] Soummer, R., Pueyo, L., and Larkin, J., "DETECTION AND CHARACTERIZATION OF EXOPLANETS AND DISKS USING PROJECTIONS ON KARHUNEN-LOÈVE EIGENIMAGES," *The Astrophysical Journal* **755**, L28 (Aug. 2012).

[4] Marois, C., Lafreniere, D., Doyon, R., Macintosh, B., and Nadeau, D., "Angular Differential Imaging: A Powerful High-Contrast Imaging Technique," *The Astrophysical Journal* **641**, 556–564 (Apr. 2006).

[5] N'Diaye, M., Soummer, R., Pueyo, L., Carlotti, A., Stark, C. C., and Perrin, M. D., "APODIZED PUPIL LYOT CORONAGRAPHS FOR ARBITRARY APERTURES. V. HYBRID SHAPED PUPIL DESIGNS FOR IMAGING EARTH-LIKE PLANETS WITH FUTURE SPACE OBSERVATORIES," *The Astrophysical Journal* **818**, 163 (Feb. 2016).

[6] Zimmerman, N. T., Eldorado Riggs, A. J., Jeremy Kasdin, N., Carlotti, A., and Vanderbei, R. J., "Shaped pupil Lyot coronagraphs: high-contrast solutions for restricted focal planes," *Journal of Astronomical Telescopes, Instruments, and Systems* **2**, 011012 (Jan. 2016).

[7] Riggs, A. J. E., Zimmerman, N., Carlotti, A., Kasdin, N. J., and Vanderbei, R., "Shaped pupil design for future space telescopes," 914325 (Aug. 2014).

[8] Blaurock, C., McGinnis, M., Kim, K., and Mosier, G. E., "Structural-thermal-optical performance (STOP) sensitivity analysis for the James Webb Space Telescope," 58670V (Aug. 2005).

[9] Mendillo, C. B., Howe, G. A., Hewawasam, K., Martel, J., Finn, S. C., Cook, T. A., and Chakrabarti, S., "Optical tolerances for the PICTURE-C mission: error budget for electric field conjugation, beam walk, surface scatter, and polarization aberration," in [*Techniques and Instrumentation for Detection of Exoplanets VIII*], Shaklan, S., ed., 34, SPIE, San Diego, United States (Sept. 2017).

[10] Stover, J. C., [*Optical scattering. Measurement and analysis*] (Jan. 1995). Publication Title: SPIE Press Volume ADS Bibcode: 1995osma.book.....S.

[11] Guyon, O., "Extreme Adaptive Optics," *Annual Review of Astronomy and Astrophysics* **56**, 315–355 (Sept. 2018). Publisher: Annual Reviews.

[12] Oppenheimer, B. R. and Hinkley, S., "High-Contrast Observations in Optical and Infrared Astronomy," *Annual Review of Astronomy and Astrophysics* **47**, 253–289 (Sept. 2009).

[13] Krist, J. E., Gutt, G., Marchen, L., McGuire, J., Amiri, N., Nemati, B., Saini, N., Tang, H., Riggs, A., Marx, D., Sidick, E., and Zhou, H., "WFIRST coronagraph optical modeling," in [*Techniques and Instrumentation for Detection of Exoplanets VIII*], Shaklan, S., ed., 4, SPIE, San Diego, United States (Sept. 2017).

[14] Trauger, J. T., Moody, D. C., Krist, J. E., and Gordon, B. L., "Hybrid Lyot coronagraph for WFIRST-AFTA: coronagraph design and performance metrics," *Journal of Astronomical Telescopes, Instruments, and Systems* **2**, 011013 (Jan. 2016). Publisher: SPIE.

[15] Riggs, A. E., Ruane, G., Coker, C. T., Shaklan, S. B., Sidick, E., Jewell, J. B., Mawet, D., Balasubramanian, K., and Stark, C. C., "Fast linearized coronagraph optimizer (FALCO) IV: coronagraph design survey for obstructed and segmented apertures," in [*Space Telescopes and Instrumentation 2018: Optical, Infrared, and Millimeter Wave*], MacEwen, H. A., Lystrup, M., Fazio, G. G., Batalha, N., Tong, E. C., and Siegler, N., eds., 167, SPIE, Austin, United States (Aug. 2018).

[16] Groff, T. D., Eldorado Riggs, A. J., Kern, B., and Jeremy Kasdin, N., "Methods and limitations of focal plane sensing, estimation, and control in high-contrast imaging," *Journal of Astronomical Telescopes, Instruments, and Systems* **2**, 011009 (Dec. 2015).

[17] Pueyo, L., Kay, J., Kasdin, N. J., Groff, T., McElwain, M., Give'on, A., and Belikov, R., "Optimal dark hole generation via two deformable mirrors with stroke minimization," *Applied Optics* **48**, 6296 (Nov. 2009).

[18] Give'on, A., Kern, B., Shaklan, S., Moody, D. C., and Pueyo, L., "Broadband wavefront correction algorithm for high-contrast imaging systems," 66910A (Sept. 2007).

[19] Perrin, M., Long, J., Douglas, E., Sivaramakrishnan, A., Slocum, C., and others, "POPPY: Physical Optics Propagation in PYthon," *Astrophysics Source Code Library* , ascl:1602.018 (Feb. 2016). ADS Bibcode: 2016ascl.soft02018P.

[20] Por, E. H., Haffert, S. Y., Radhakrishnan, V. M., Doelman, D. S., van Kooten, M., and Bos, S., "High Contrast Imaging for Python (HCIPy): an open-source adaptive optics and coronagraph simulator," in [*Adaptive Optics Systems VI*], Schmidt, D., Schreiber, L., and Close, L. M., eds., 152, SPIE, Austin, United States (July 2018).

[21] Everhart, E. and Kantorski, J. W., "Diffraction patterns produced by obstructions in reflecting telescopes of modest size," *The Astronomical Journal* **64**, 455 (Dec. 1959).

[22] Richter, J. L., "Spider diffraction: a comparison of curved and straight legs," *Applied Optics* **23**, 1907 (June 1984).

[23] Gaskill, J. D., [*Linear Systems, Fourier Transforms, and Optics*] (Jan. 1978). Publication Title: Linear Systems ADS Bibcode: 1978lsft.book.....G.

[24] Breckinridge, J. B., Harvey, J. E., Hull, T., and Crabtree, K., "Exoplanet telescope diffracted light minimized: the pinwheel-pupil solution," in [*Space Telescopes and Instrumentation 2018: Optical, Infrared, and Millimeter Wave*], MacEwen, H. A., Lystrup, M., Fazio, G. G., Batalha, N., Tong, E. C., and Siegler, N., eds., 61, SPIE, Austin, United States (July 2018).

[25] Breckinridge, J. B., Harvey, J., Irvin, R. G., Chipman, R. A., Kupinski, M., Davis, J., Kim, D. W., Ewan, D. S., Lillie, C. F., and Hull, T. B., "Stealth telescopes for space and ground astronomy," in [*UV/Optical/IR Space Telescopes and Instruments: Innovative Technologies and Concepts IX*], Breckinridge, J. B., Stahl, H. P., and Barto, A. A., eds., 17, SPIE, San Diego, United States (Sept. 2019).

[26] Irvin, R. G., Harvey, J. E., Pfisterer, R. N., and Breckinridge, J. B., "Novel designs for minimizing diffraction effects of large segmented mirror telescopes," in [*Current Developments in Lens Design and Optical Engineering XIX*], Johnson, R. B., Mahajan, V. N., and Thibault, S., eds., 19, SPIE, San Diego, United States (Sept. 2018).

[27] Feng, Y.-T., Ashcraft, J., Breckinridge, J., Harvey, J., Douglas, E., Choi, H., Lillie, C., Hull, T., and Kim, D. W., "Topological pupil segmentation and point spread function analysis for large aperture imaging systems," in [*AOPC 2020: Optics Ultra Precision Manufacturing and Testing*], Zhang, D., Kong, L., and Luo, X., eds., 24, SPIE, Beijing, China (Nov. 2020).

[28] Breckinridge, J. B., Hull, T. B., and Harvey, J. E., "Innovative aperture segmentations control image plane diffraction," in [*International Conference on Space Optics — ICSO 2020*], Sodnik, Z., Cugny, B., and Karafolas, N., eds., 179, SPIE, Online Only, France (June 2021).

[29] Pueyo, L., Zimmerman, N., Bolcar, M., Groff, T., Stark, C., Ruane, G., Jewell, J., Wang, J., Redding, D., Mazoyer, J., Fograty, K., Juanola-Parramon, R., Domagal-Goldman, s., Roberge, A., Mandell, A., Guyon, O., Soummer, R., and St Laurent, K., "The LUVOIR architecture "A" coronagraph instrument," in [*UV/Optical/IR Space Telescopes and Instruments: Innovative Technologies and Concepts VIII*], MacEwen, H. A. and Breckinridge, J. B., eds., 15, SPIE, San Diego, United States (Sept. 2017).

[30] Mawet, D., Serabyn, E., Liewer, K., Burruss, R., Hickey, J., and Shemo, D., "THE VECTOR VORTEX CORONAGRAPH: LABORATORY RESULTS AND FIRST LIGHT AT PALOMAR OBSERVATORY," *The Astrophysical Journal* **709**, 53–57 (Jan. 2010).

[31] Soummer, R., "Apodized Pupil Lyot Coronagraphs for Arbitrary Telescope Apertures," *The Astrophysical Journal* **618**, L161–L164 (Jan. 2005).

[32] Guyon, O., Kern, B., Belikov, R., Bryson, S., Sirbu, D., and Bendek, E. A., "Design and performance analysis of a PIAACMC coronagraph on a segmented aperture," in [*Space Telescopes and Instrumentation 2018: Optical, Infrared, and Millimeter Wave*], MacEwen, H. A., Lystrup, M., Fazio, G. G., Batalha, N., Tong, E. C., and Siegler, N., eds., 52, SPIE, Austin, United States (Aug. 2018).